Journal of
Composites Science

Article

Effects of the Rate Dependency of a Matrix Material on the Tensile Response of Plain Weave Carbon Fabric Reinforced Epoxy Composites

Taeseong Choi and Wooseok Ji *

Department of Mechanical Engineering, Ulsan National Institute of Science and Technology (UNIST), Ulsan 44919, Republic of Korea
* Correspondence: wsji@unist.ac.kr

Abstract: Textile composites are extensively used in structures subjected to both static and dynamic loads. However, research on how loading rates influence performance remains limited. A better understanding of how the rate dependency of matrix materials affects the mechanical behavior of textile composites could facilitate more accurate performance predictions and the efficient selection of components based on loading rates. This study investigates the effect of the rate dependency of epoxy on the overall rate dependency of a plain weave carbon fabric-reinforced epoxy composite. Specimens were prepared using only epoxy resin, and tensile tests were conducted at four loading rates (5 mm/min, 50 mm/min, 200 mm/min, and 800 mm/min) to evaluate changes in the tensile properties of epoxy with varying loading rates. Composite specimens were fabricated using the same epoxy, and tensile tests were performed under identical conditions. The results demonstrated that both materials became more brittle at higher loading rates while their stiffness remained largely unaffected. Furthermore, the failure process of the composite at different loading rates was analyzed through micro-scale finite element analysis. The analysis revealed that the onset of failure in textile composites shifted owing to the rate-dependent brittleness of epoxy. To mitigate the high computational cost of explicit simulations accounting for time dependency, a modified Johnson–Cook model and an acceleration model were newly developed and incorporated into the analysis.

Keywords: rate dependency; epoxy material; textile composites; finite element analysis

check for updates

Academic Editor: Traian Dumitrica

Received: 25 November 2024
Revised: 20 December 2024
Accepted: 8 January 2025
Published: 9 January 2025

Citation: Choi, T.; Ji, W. Effects of the Rate Dependency of a Matrix Material on the Tensile Response of Plain Weave Carbon Fabric Reinforced Epoxy Composites. *J. Compos. Sci.* **2025**, *9*, 29. https://doi.org/10.3390/jcs9010029

1. Introduction

Composite materials have become essential in various industries owing to their high strength-to-weight ratio. Composites with different fiber architectures have been developed to meet the mechanical property requirements of different applications. For example, unidirectional fiber-reinforced composites, with fibers aligned in a single direction, offer high strength and stiffness along that direction. In contrast, short fiber-reinforced composites featuring randomly arranged short fibers are more versatile for complex-shaped components and have lower production costs. Among these, textile fabric-reinforced composites are widely used in advanced fields such as aerospace and automotive industries, where high reliability is critical, owing to their exceptional impact and fatigue resistance [1–3]. As a result, textile composites are frequently exposed to conditions involving impacts and fatigue, encompassing a wide range of loading rates. Given that the mechanical behavior of textile composites varies with loading rates, numerous studies have investigated their rate-dependent properties [4–10]. Naik et al. [7] demonstrated that the tensile strength of woven glass/epoxy composites increases with higher loading rates. Similarly, Fitoussi et al. [8] reported that while the tensile strength of woven carbon/epoxy composites increases with loading rate, the tensile stiffness shows minimal variation. In contrast, Zhang et al. [9] and Lu [10] observed that both the tensile strength and stiffness of woven carbon/epoxy composites increase with increasing loading rates.

Experimentally verifying the rate dependency of textile composites for all combinations of constituent materials is time-consuming and costly. Consequently, some studies have focused on predicting the rate-dependent mechanical properties of textile composites based on the rate dependency of their constituent materials. Ma et al. [11] analyzed changes in the tensile strength of plain weave R-glass/epoxy composites by considering the increased tensile strength of R-glass fiber and epoxy with increasing loading rates. Similarly, Ehsan et al. [12] examined the changes in the mechanical tensile strength of plain weave glass/epoxy composites, accounting for the increased tensile strength of glass fiber and epoxy at higher loading rates. However, these studies did not distinctly isolate the independent effect of the matrix material's rate dependency on the behavior of textile composites, as they analyzed the rate dependency of both fiber and matrix materials together. A clearer understanding of the independent influence of the matrix material's rate dependency on the mechanical behavior of textile composites would enable more efficient material selection and performance prediction when designing textile composites for varying loading rates.

In this study, the effect of the rate dependency of a matrix material on textile composites was analyzed. First, tensile tests were performed on both the textile composites and epoxy, which were fabricated using the same resin system and curing process at four different loading rates. A widely adopted plain weave textile fabric fabricated with the Toray T300 fiber [13], which exhibits rate-independent mechanical behavior, was used. Second, a micro-scale finite element analysis (FEA) of the composite was conducted, employing a rate-dependent material model for epoxy. To mitigate the high computational cost of explicit/dynamic analysis that accounts for time dependency, a modified Johnson–Cook model and an acceleration model were developed and incorporated into the analysis.

This paper is structured as follows: Section 2 introduces the materials and test methods used in the experiments. Section 3 describes the micro-scale finite element (FE) model developed based on the observed results. Section 4 presents the test results, FEA findings, and associated discussions. Finally, Section 5 summarizes the key findings of this study and presents the conclusions.

2. Experimental Setup

2.1. Materials and Specimen

The epoxy used in this study was the INF114 resin and INF211 hardener from PRO-SET® Inc. (Bay City, MI, USA) The 1321P plain woven fabric from JMC Corp (Tokyo, Japan), woven with Toray® Inc's T300 3K carbon fiber (Tokyo, Japan), was used. Since the mechanical behavior of both composites and epoxy varies depending on the resin system and curing process [14,15], all specimens were fabricated using the same resin system and curing process.

The epoxy specimens were produced by mixing the resin and hardener in a weight ratio of 3.65:1. The mixed resin system was poured into a mold, allowed a 3 h gel time, and then thermally cured at 82 °C for 8 h. Composite panels were fabricated by stacking 13 layers of plain weave carbon fabric in the same direction and injecting the mixed resin system using the vacuum-assisted resin transfer molding method. These composite panels underwent the same curing process as the epoxy specimens and were then cut into specimen shapes using a waterjet. The specimen configuration based on ASTM D638-14 [16] is shown in Figure 1.

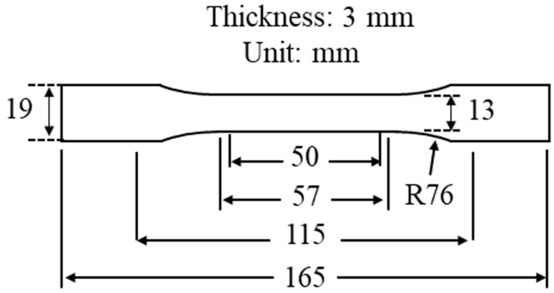

Figure 1. Configuration of the specimen.

2.2. Tensile Test Setup

Tensile tests were conducted using the INSTRON 5982 universal testing machine. The loading rates were set at 5 mm/min, 50 mm/min, 200 mm/min, and 800 mm/min, with the tests at each loading rate labeled as S5, S50, S200, and S800, respectively. The minimum and maximum loading rates were selected based on the recommendation of ASTM D638-14 and the maximum loading rate of the INSTRON 5982 device. All tensile tests were repeated three times. The tensile test setup is shown in Figure 2a. Stress was measured using a load cell attached to the universal testing machine. The strain was measured with an extensometer; however, for the composite at S800, the extensometer slipped on the specimen surface, preventing strain measurement. As a result, strain for this sample was measured by the digital image correlation method [17] using a high-speed camera (Photron Fastcam SA-Z), as shown in Figure 2b.

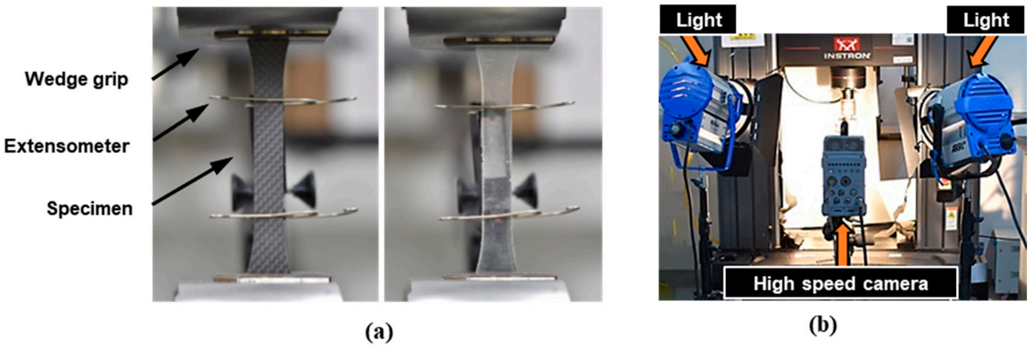

Figure 2. (**a**) Tensile test setup and (**b**) DIC setup for composite at S800.

3. FE Model

The purpose of FEA in the presented study was to find a qualitative explanation about the rate-dependency of the textile composite at its constituent level. Hence, the microstructural geometry of the textile composite was simplified to construct a micromechanics finite element (FE) model. The simplified micromechanics FE model is described in Section 3.1. In the FE model, the carbon fiber was modeled as an isotropic elastic material while the epoxy was modeled as an isotropic elasto-plastic material. The plasticity of the epoxy was modeled using the Johnson–Cook plasticity (JCP) model. The damage behaviors of the carbon fiber and epoxy were modeled with the Johnson–Cook damage (JCD) model. The material models are described in Section 3.2. Especially, the JCD model was modified to accelerate the transient analysis in the real-time domain. This acceleration model is explained in Section 3.3. ABAQUS/Explicit was used for the finite element analysis.

3.1. Geometry and Boundary Conditions

A simplified unit cell model of the composite was created by photographing its cross-section before the tensile test, as shown in Figure 3. The width of the tow, as measured in Figure 3, was 1.65 mm, and the height was 0.15 mm. The fiber diameter was 7 µm, and the fiber volume fraction, determined through a matrix burn-out test in accordance with ASTM D2584, was found to be 52.8% [18].

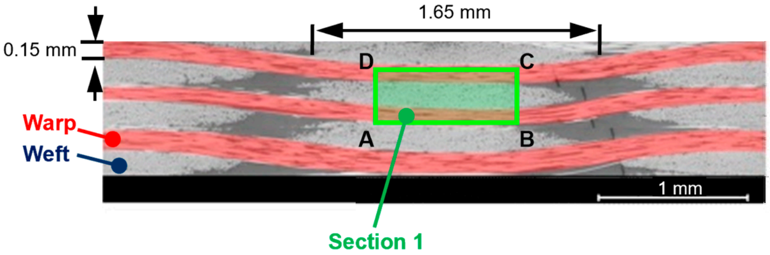

Figure 3. Cross-section image of the composite before the tensile test.

Figure 4 shows the geometry of the simplified unit cell model designed to analyze the progressive failure pattern of the composite. The length of the geometry model was set to 0.96 mm, approximately half the width of the weft (1.65 mm). The height of a single layer was set to 0.17 mm, which included the measured tow height of 0.15 mm and an additional thin epoxy layer of 0.01 mm on each side, resulting in a total geometry model height of 0.34 mm. To clearly capture the effect of the matrix's rate dependency on the composite, the matrix and fibers within the tow were modeled separately. Considering computational efficiency, the fiber diameter was scaled from 7 µm to 70 µm, and the diameter of the central fiber in the weft was increased to 100 µm to induce stress concentration and initiate failure. The spacing between fibers was adjusted to ensure that the fiber volume fraction of the geometry model closely matched the measured value of 52.8%, resulting in a fiber volume fraction of 50.6% in the model. To minimize thickness, the thickness in the geometry model was set to 8 mm, sufficient to accommodate a single fiber. The model used a total of 12,994 eight-node brick elements with reduced integration. This element type performs better than four-node tetrahedral elements while balancing computational efficiency and accuracy [19].

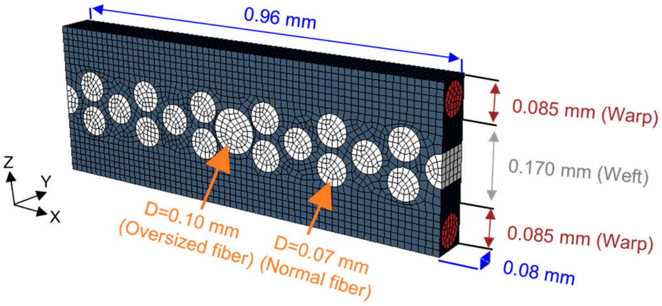

Figure 4. Geometry model of FEA for composite.

To simulate tensile tests at varying speeds, the boundary conditions were set, as shown in Figure 5. At point F, displacements in both the Y and X directions were constrained to 0, preventing global movement of the FE model in these directions. At point E, displacement in the Z direction was also constrained to prevent the global rotation of the FE model around the X-axis. By applying the condition $U_x = 0$ to face AFED, global movement in the X direction, as well as global rotations around the Y and Z axes, was restricted. A uniform tensile speed in the X direction was applied to face BGHC to simulate the tensile behavior.

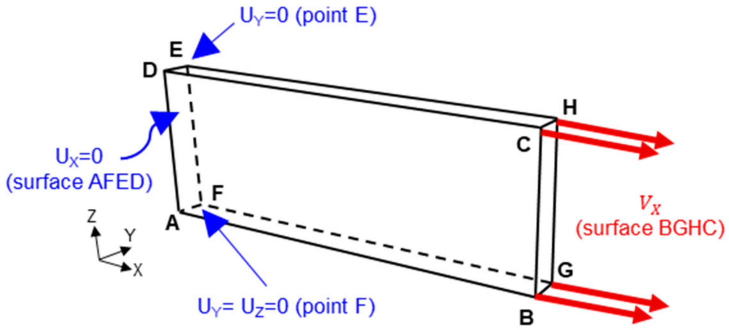

Figure 5. Boundary conditions of the FEA for composite.

3.2. Material Model

Figure 6 shows the stress–strain curve illustrating the failure growth mechanism. Epoxy was modeled as an isotropic elasto-plastic material, where material failure initiates at point c after passing through the elastic region (a–b) and plastic region (b–c). The widely used Johnson–Cook plasticity model [20] was employed to model plastic behavior. The JCP model was used for the epoxy material mainly because of its distinct nonlinear behavior, which is shown in Section 4. The JCP model has already been used by many researchers for modeling the nonlinearity of epoxy materials [21–23]. In addition, the JCP model was useful to consider the rate dependency with the JCD model, which also considers material behavior changes according to strain rates.

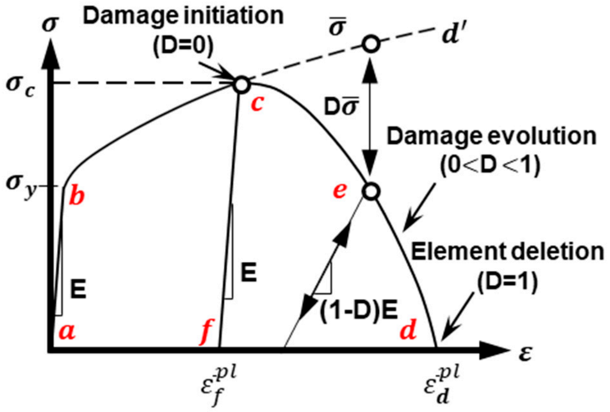

Figure 6. Stress–strain curve representing damage evolution mechanisms.

In this study, the JCP model was applied without considering the effects of temperature, focusing exclusively on the influence of strain rate on plastic behavior. The model is expressed as shown in Equation (1).

$$\bar{\sigma} = \left[A + B\left(\bar{\varepsilon}^{pl}\right)^{n}\right] \tag{1}$$

Here, $\bar{\sigma}$ represents the equivalent stress, A is the initial yield stress, B is the hardening coefficient, $\bar{\varepsilon}^{pl}$ is the equivalent plastic strain, and n is the strain hardening exponent.

The point c in Figure 6, where failure begins, can be relocated in accordance with the loading rate. The Johnson–Cook damage model [24] accounts for the changes in failure strain with varying loading rates. The following is the equation for rate-dependent failure initiation:

$$\bar{\varepsilon}_f^{pl} = D_1\left[1 + D_2 ln\left(\dot{\bar{\varepsilon}}_f^{pl} / \dot{\bar{\varepsilon}}_{f0}^{pl}\right)\right] \tag{2}$$

Here, $\bar{\varepsilon}_f^{pl}$ represents the $\bar{\varepsilon}^{pl}$ at which damage is initiated, and $\dot{\bar{\varepsilon}}_f^{pl}$ and $\dot{\bar{\varepsilon}}_{f0}^{pl}$ are the equivalent plastic strain rate at damage initiation and the reference equivalent plastic strain rate, respectively. D_1 is $\bar{\varepsilon}_f^{pl}$ when $\dot{\bar{\varepsilon}}_f^{pl} = \dot{\bar{\varepsilon}}_{f0}^{pl}$, and D_2 is the scaling factor for $\bar{\varepsilon}_f^{pl}$ as a function of $\dot{\bar{\varepsilon}}_f^{pl}$. Once the damage is initiated and propagates into the c-d region of Figure 6, the damage variable (D) begins to increase. D indicates the extent of damage and evolves from 0 to 1 as damage progresses. The evolution of D is computed from

$$D = \left(\bar{\varepsilon}^{pl} - \bar{\varepsilon}_f^{pl}\right) / \left(\bar{\varepsilon}_d^{pl} - \bar{\varepsilon}_f^{pl}\right) \tag{3}$$

where $\bar{\varepsilon}_d^{pl}$ is the equivalent plastic strain at complete failure. As the damage variable D increases, the stress is reduced by $D\bar{\sigma}$ as indicated in Figure 6. This reflects the progressive decrease in stress as failure progresses. Simultaneously, the elastic modulus is reduced to $(1 - D)E$. In Equation (3), D becomes 1 when $\bar{\varepsilon}^{pl}$ reaches $\bar{\varepsilon}_d^{pl}$, and the element is deleted. $\bar{\varepsilon}_d^{pl}$ is calculated from

$$G_{IC} = \int_{\bar{\varepsilon}_f^{pl}}^{\bar{\varepsilon}_d^{pl}} \bar{\sigma} L_{ch} d\bar{\varepsilon}^{pl} \tag{4}$$

where G_{IC} represents the fracture energy, and L_{ch} is the characteristic element length of each element. The same damage model without a b–c plastic deformation region in Figure 6 was utilized for the carbon fibers. They are known to exhibit only elastic behavior without plastic deformation prior to failure [13].

3.3. Acceleration Model

The velocity loading V_X in Figure 5 was computed from

$$V_X = L \times \dot{\varepsilon}_{test} \tag{5}$$

where L is the length of the FE model along the loading direction, and $\dot{\varepsilon}_{test}$ is the strain rate. Here, $\dot{\varepsilon}_{test}$ was calculated by averaging the rate of strain change measured during the test and dividing it by its data acquisition rate.

Typically, dynamic simulations based on explicit time integration are computationally expensive owing to tiny time increments for numerical stability. To improve computational efficiency, an acceleration coefficient α was introduced

$$\alpha = \dot{\varepsilon}_{FEM} / \dot{\varepsilon}_{test} \tag{6}$$

where $\dot{\varepsilon}_{FEM}$ is a user-defined accelerated strain rate used in FEA. α was inserted in Equation (2) and modified the JCD model such that

$$\bar{\varepsilon}_f^{pl} = D_1 \left[1 + D_2 ln\left(\dot{\bar{\varepsilon}}_f^{pl} / \alpha \dot{\bar{\varepsilon}}_{f0}^{pl}\right)\right] \tag{7}$$

The velocity loading V_X in Equation (5) was accordingly switched to

$$V_X = L \times \dot{\varepsilon}_{FEM} \tag{8}$$

The practical applications of using α and $\dot{\varepsilon}_{FEM}$ are explained in Section 4.3.2.

4. Results and Discussion

4.1. Test Results of the Epoxy

Figure 7 displays the representative tensile stress–strain curves of epoxy at different loading rates, while Figure 8 shows the corresponding variations in material properties. As seen in Figure 7, epoxy exhibits a notable increase in brittleness with higher loading rates, though stiffness remains largely unaffected. Figure 8a illustrates the change in tensile strength, with a steady decrease from 76.0 MPa at S5 to 57.8 MPa at S800, representing an approximate reduction of 24%. Figure 8b demonstrates that the elongation decreases by approximately 48%, from 3.98% to 1.89%, as the loading rate increases, further emphasizing the marked increase in brittleness. Figure 8c shows the variation in elastic modulus with loading rate. Stiffness increases slightly from 2.98 GPa at S5 to 3.17 GPa at S800, representing an approximately 6% increase, which is negligible compared to the 24% and 48% reductions in tensile strength and elongation, respectively. Together, Figures 7 and 8 confirm that while stiffness remains largely unchanged with increasing loading rates, both tensile strength and elongation decrease significantly, thereby amplifying the brittleness of the material.

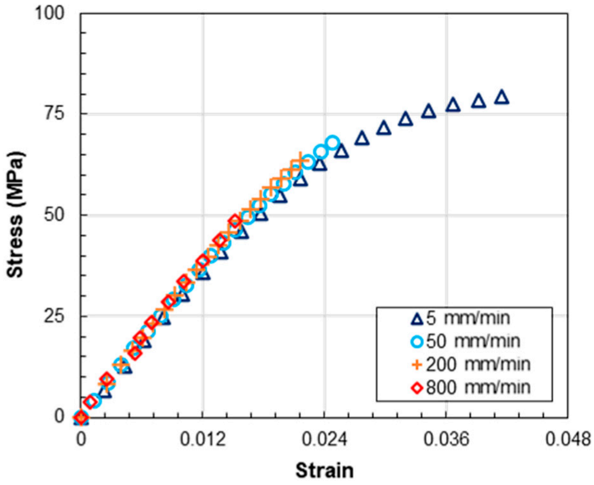

Figure 7. Representative tensile strain–tensile stress curves of the epoxy at different loading rates.

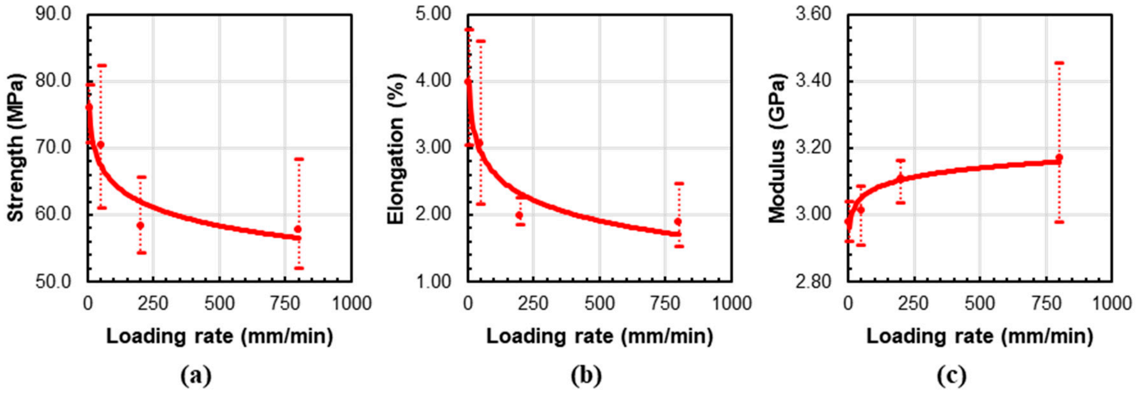

Figure 8. Tensile material properties of the epoxy at different loading rates: (**a**) strength, (**b**) elongation, and (**c**) modulus.

To examine the changes in the fracture surface of epoxy with varying loading rates, the fracture surfaces of epoxy specimens were photographed, as shown in Figure 9. Upon fracturing, epoxy forms mirror, mist, and hackle regions. The mirror region, a smooth area at the crack initiation point, marks the area where the crack begins to propagate and gradually accelerates, eventually becoming unstable. As the crack propagates further, it leaves behind rough surfaces, creating the mist and hackle regions. Cantwell et al. [25]

explored the relationship between the reduction in mirror region size and the decrease in material fracture toughness. A smaller mirror region suggests that the material undergoes unstable deformation during fracture, indicating a reduction in fracture toughness. As seen in Figure 9, the mirror region size diminishes with increasing loading rates, suggesting that at higher loading rates, epoxy experiences unstable deformation and a corresponding decrease in toughness.

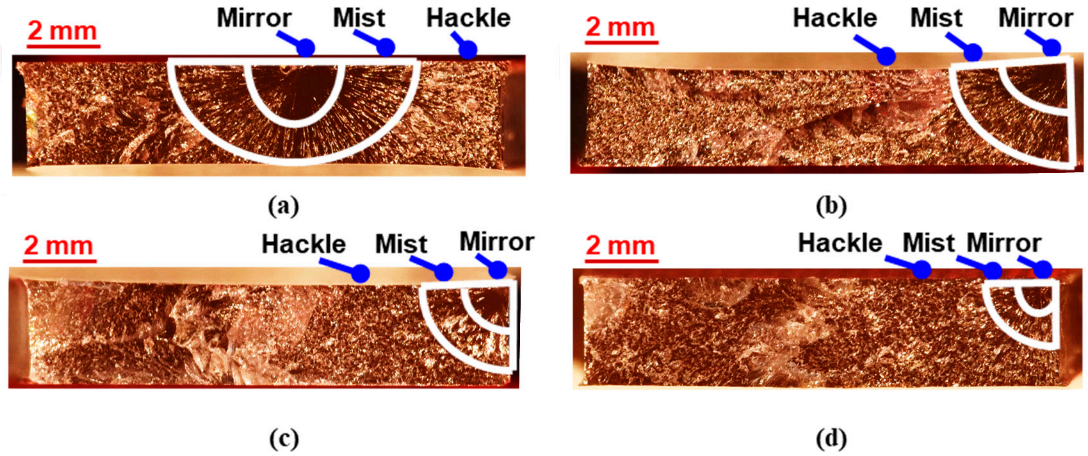

Figure 9. Fracture surface of the epoxy at loading rates of (**a**) 5 mm/min, (**b**) 50 mm/min, (**c**) 200 mm/min, and (**d**) 800 mm/min.

4.2. Test Results of Composite

Figure 10 presents the representative tensile stress–strain curves of the composite at different loading rates, while Figure 11 illustrates the corresponding variations in material properties. The maximum stress consistently decreases, similar to the epoxy. The tensile strength of the textile composites decreases from 564 MPa at S5 to 526 MPa at S800, approximately by 7%. The tensile strength of the epoxy material decreases from 76.0 MPa at S5 to 57.8 MPa at S800, approximately by 24%. Likewise, the elongation of the composite decreases as the loading rate increases. The maximum elongation of the textile composite slightly decreases from 0.94% at S5 to 0.88% at S800. The maximum elongation of the epoxy decreases from 3.98% at S5 to 1.89% at S800. The reduction percentages of the composite and epoxy are about 6% and 48%, respectively. The stiffness of the textile composite remains nearly constant, as shown in Figure 11. It increases from 62.56 GPa at S5 to 63.83 GPa at S50, then decreases to 62.23 GPa at S200 before increasing again to 62.89 GPa at S800. The stiffness of the epoxy increases about 6% from 2.98 GPa at S5 to 3.17 GPa at S800. Based on Figures 10 and 11, it can be concluded that, similar to epoxy, the composite exhibits increasing brittleness with increasing loading rates despite no significant changes in stiffness. However, the changes are not as significant as those of the epoxy material, probably because of the rate-insensitive carbon fibers.

To examine changes in the failure pattern of the composite with varying loading rates, the fractured specimens were cut along the cutting plane after testing, as shown in Figure 12a. The fracture surface, marked in green, was then observed. Figure 12b shows the fracture surface of the composite at S5. In both Figure 12b,c, the red-marked areas represent the weft tow, while the blue-marked areas indicate the warp tow. These colored regions roughly outline the fibers separated based on the observed fracture surface. As shown in Figure 12b, at S5, the fracture surface formed perpendicular to the loading direction, with no additional damage observed outside the fracture surface. Figure 12c displays the fracture surface of the composite at S800, where, similar to S5, the fracture surface remains perpendicular to the loading direction, and no additional damage is evident outside the fracture surface.

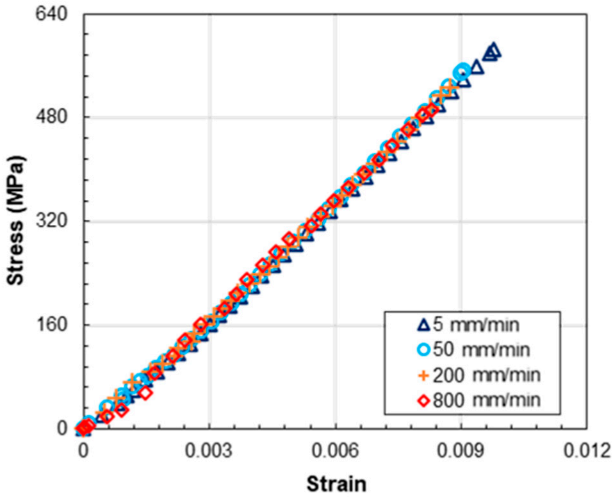

Figure 10. Representative tensile strain–tensile stress curves of composites at different loading rates.

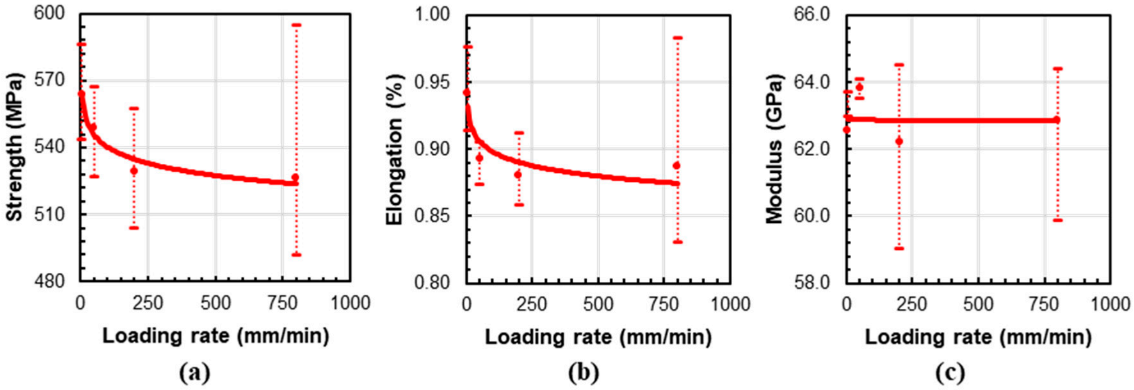

Figure 11. Tensile material properties of the composite at different loading rates: (**a**) strength, (**b**) elongation, and (**c**) modulus.

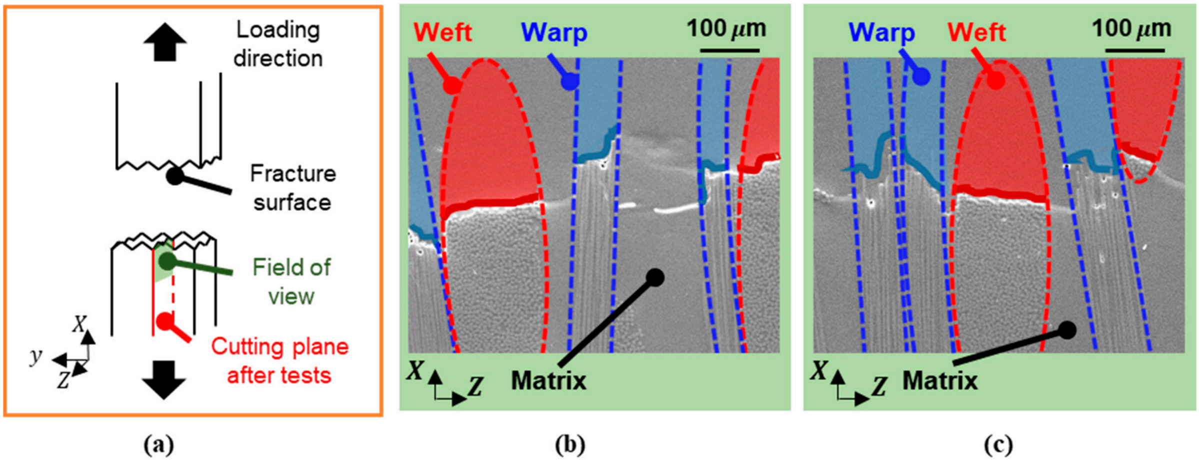

Figure 12. (**a**) Schematic of the field of view, (**b**) fracture surface of the composite at S5, and (**c**) fracture surface of the composite at S800.

To examine the failure modes within the warp and weft tows, the fracture surface captured in Figure 12 was magnified and photographed, as shown in Figure 13. Figure 13a presents a magnified view of the weft tow fracture surface from Figure 12b, revealing that no fiber breakage occurred in the weft tow; only matrix cracking was observed. Figure 13b shows a magnified image of the warp tow fracture surface from Figure 12b. In this image, the matrix crack seen in Figure 13a propagates toward the warp tow but does not extend further. However, fiber breakage, absent in the weft tow, occurs within the warp tow, leading to its separation.

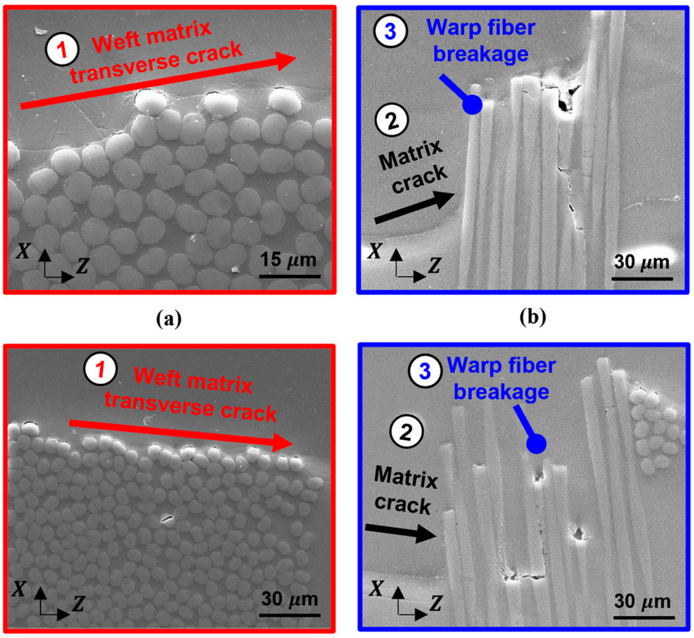

(a) (b) (c) (d)

Figure 13. Fracture surface of the composite: (**a**) weft tow at S5, (**b**) warp tow at S5, (**c**) weft tow at S800, and (**d**) warp tow at S800.

Figure 13 provides a magnified view of the weft tow fracture surface at S800, derived from Figure 12. Similarly to earlier observations, no fiber breakage was detected in the weft tow, with only matrix cracking present. Figure 13d depicts a magnified view of the warp tow fracture surface at S800, also from Figure 12, confirming that, as with S5, the fracture at S800 resulted from fiber breakage in the warp tow.

From Figures 12 and 13, it was confirmed that regardless of the loading rate, the weft tow fails through matrix cracking rather than fiber breakage, while the warp tow fails owing to fiber breakage, resulting in fractures perpendicular to the loading direction.

4.3. Results of FEA

4.3.1. Material Parameters

The material properties governing the elasto-plastic behavior of each material are summarized in Table 1, while the damage material properties are presented in Table 2. Figure 14a displays the $\bar{\varepsilon}^{pl}$–$\dot{\bar{\varepsilon}}^{pl}$ curve of the epoxy at each loading rate. When the loading rate is constant, the strain rate remains steady; however, the plastic strain rate gradually increases as deformation progresses. $\dot{\bar{\varepsilon}}_f^{pl}$ and $\bar{\varepsilon}_f^{pl}$ for each loading rate were calculated as $\dot{\bar{\varepsilon}}^{pl}$ and $\bar{\varepsilon}^{pl}$ at the failure point, respectively. For S5, $\dot{\bar{\varepsilon}}_f^{pl}$ (6.09×10^{-4}/s) was calculated as $\dot{\bar{\varepsilon}}_{f0}^{pl}$, and $\bar{\varepsilon}_f^{pl}$ (0.0145) at S5 was calculated as D_1. To determine D_2, $\dot{\bar{\varepsilon}}_f^{pl}$ and $\bar{\varepsilon}_f^{pl}$ for each loading rate were analyzed, and using Equation (2), the D_2 fitting curve was plotted, as shown in Figure 14b. The slope of the D_2 fitting curve, calculated as -0.2972, was determined as D_2.

Table 1. Elasto-plastic material properties of the carbon fiber and epoxy.

Material	ρ (kg/m^3)	E (GPa)	ν	A (MPa)	B (MPa)	n
Epoxy	1140	3.07	0.37 [18]	52.5	110	0.35
Carbon fiber	1760 [26]	230 [26]	0.2 [18]	3540 [26]	0	0

Table 2. Damage material properties of the carbon fiber and epoxy.

Material	D_1	D_2	G_{IC}
Epoxy	0.0145	−0.2972	0.06 N/mm [27]
Carbon fiber	10^{-6}	0	0.006 N/mm [28]

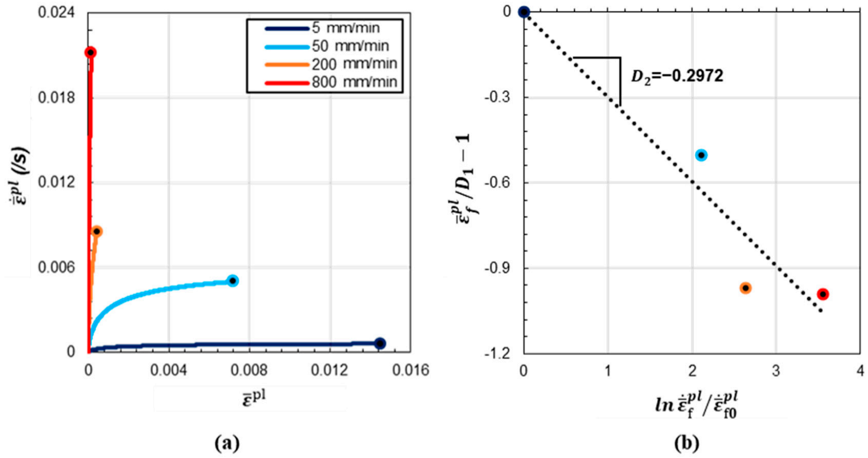

Figure 14. (**a**) Equivalent plastic strain rate–equivalent plastic strain curve (**b**) D_2 fitting curve.

4.3.2. Validation of the Material Model

A single-element analysis of the epoxy was conducted to verify whether the material model accurately reflected the test results. The analysis was carried out using the dynamic/explicit module of the commercial software ABAQUS 2021, employing a 1 × 1 × 1 mm eight-node brick element with reduced integration. The boundary conditions were applied as shown in Figure 15 with different loading rates controlled by V_X. The velocity V_X was determined by multiplying the element length by a desired strain rate. Table 3 lists the strain rates corresponding to the four loading rates and total analysis times. In Table 3, $\dot{\varepsilon}_{test}$ refers to the strain rate measured from the epoxy tensile test at a specific loading rate and $\dot{\varepsilon}_{FEM}$ is the user-defined strain rate for accelerated simulations. For the validation analysis, $\dot{\varepsilon}_{FEM}$ was set to 1/s as listed in Table 3. The α values in Table 3 were calculated according to Equation (6). $T_\alpha^{\otimes}$ and $T_\alpha^{\circledcirc}$ in Table 3 represents the analysis time without and with α, respectively.

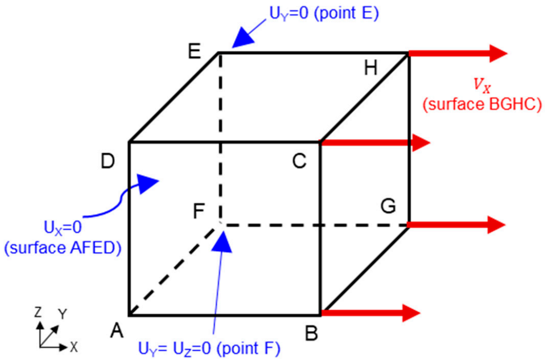

Figure 15. Boundary conditions of single-element simulation for the epoxy.

Table 3. Acceleration factor of the single-element simulation for the epoxy.

Loading Rate (mm/min)	$\dot{\varepsilon}_{test}$ (10^{-4}/s)	$\dot{\varepsilon}_{FEM}$ (/s)	α (10^3)	$T_{\alpha}^{\otimes}$ (s)	$T_{\alpha}^{\odot}$ (10^{-3} s)
5	7.29	1	1.37	58.4	42.6
50	65.6	1	0.15	4.95	33.0
200	252	1	0.04	1.06	26.4
800	1030	1	0.01	0.23	23.4

V_X based on $\dot{\varepsilon}_{test}$ of the 5 mm/min test, as an example, was 7.29×10^{-4} mm/s because V_X was the multiplication of the element length (1 mm) and strain rate. When this slow velocity was combined with tiny time increments for stable numerical integration, computational time was significantly increased. Instead, an $\dot{\varepsilon}_{FEM}$ of 1/s was used here to accelerate the simulation at V_X = 1 mm/s. Using $\dot{\varepsilon}_{FEM}$ and $\dot{\varepsilon}_{test}$, α was computed from Equation (6) and calibrated the damage initiation strain through Equation (7). In this way, the $\bar{\varepsilon}_f^{pl}$ from Equations (2) and (7) became the same at the two different velocities. The changes in α and analysis times for each loading rate are presented in Table 3. From Table 3 it is evident that using α in the single-element analysis reduced the analysis time by factors ranging from 10 to 1370.

Figure 16 presents the stress–strain curve of epoxy derived from the single-element simulation. In this figure, σ was calculated by dividing the tensile force applied to face BGHC by the initial height and thickness of the element, while ε was determined by dividing the tensile displacement of face BGHC by the initial width of the element. From Figure 16, it is evident that the single-element simulation effectively captured the trend of increasing brittleness with higher loading rates. Table 4 offers a quantitative comparison of material properties at varying loading rates, as obtained from both experiments and single-element simulations. The elongation and strength values observed in both experiments and simulations showed average errors of less than 5%, indicating that the material model used in this study accurately represents the experimental results.

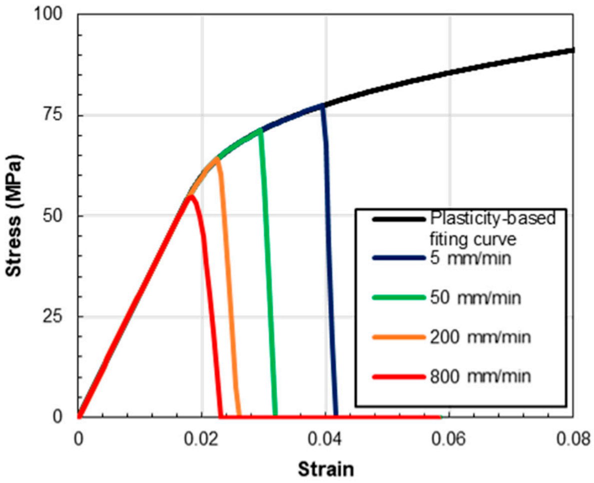

Figure 16. Stress–strain curve of single-element simulation for the epoxy.

Table 4. Comparison of material properties obtained through test and single-element simulation for the epoxy.

Loading Rate (mm/min)	Elongation [TEST] (%)	Elongation [FEM] (%)	Strength [TEST] (MPa)	Strength [FEM] (MPa)
5	3.98	3.94	76.0	77.3
50	3.07	2.96	70.4	71.2
200	1.99	2.25	58.5	64.2
800	1.89	1.84	57.8	54.6

4.3.3. FEA of Composite

In the FEA of the composite, $\dot{\varepsilon}_{FEM}$ was set to 1000/s to reduce computation time. The variations in α and analysis time for each loading rate are presented in Table 5. In Table 5 $\dot{\varepsilon}_{test}$ is the strain rates measured from the tensile tests at each loading rate. Table 5 demonstrates that incorporating α in FEA reduced the analysis time by factors ranging from approximately 3.57×10^4 to 5.43×10^6.

Table 5. Acceleration factor of FEA for composite.

Loading Rate (mm/min)	$\dot{\varepsilon}_{test}$ **(10^{-4}/s)**	$\dot{\varepsilon}_{FEM}$ **(/s)**	α **(10^4)**	$T_{\alpha}^{\otimes}$ **(s)**	$T_{\alpha}^{\odot}$ **(10^{-6} s)**
5	1.83	1000	543	81.5	15.0
50	16.7	1000	59.9	8.75	14.6
200	74.6	1000	13.4	1.90	14.2
800	280	1000	3.57	0.51	14.2

Figure 17 presents the σ–ε curves of the composite obtained from FEA. σ was calculated by dividing the tensile force applied to face BGHC by the initial height and thickness of the geometry, while ε was determined by dividing the tensile displacement of face BGHC by the initial width of the geometry. At all loading rates, the initial stiffness remains constant at approximately 65.8 GPa. However, both elongation and strength decrease as the loading rate increases. Table 6 compares the FEA and experimental results for property changes relative to the S5 loading rate. The FE results in Table 6 agree well with the experimental data. From S5 to S800, elongation decreases by approximately 7% in both the experiment and FEA, while strength decreases by approximately 6% and 7%, respectively. This demonstrates that the reduction in elongation and strength with increasing loading rates is consistently observed in both experiment and simulation.

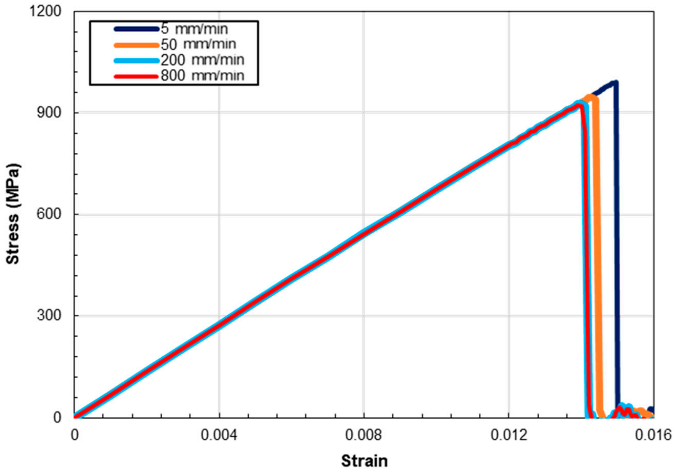

Figure 17. Stress–strain curves of composite in the FEA.

Table 6. Comparison of normalized material properties obtained through tests and FEA for the composite.

Loading Rate (mm/min)	**Normalized Elongation [TEST]**	**Normalized Elongation [FEM]**	**Normalized Strength [TEST]**	**Normalized Strength [FEM]**
5	1.00	1.00	1.00	1.00
50	0.97	0.96	0.95	0.96
200	0.94	0.94	0.94	0.93
800	0.93	0.93	0.94	0.93

Figure 18 illustrates the progressive failure pattern of the composite. The three-stage failure progression is observed from FEA consistently across all loading rates. The only difference is the strain at the failure initiation. In the initial stage, matrix cracking occurs within the weft tow. These matrix cracks cause stress concentrations in the fibers of the warp tow, leading to fiber breakage in the subsequent intermediate stage. As fiber breakage progresses, the model eventually fractures completely, perpendicular to the loading direction. At this final stage, the stress drops sharply as shown in Figure 17. The final fracture pattern in Figure 18 is aligned with the experimental observations in Figures 12 and 13. Note that the fracture patterns that were experimentally observed were also almost identical regardless of the loading rates.

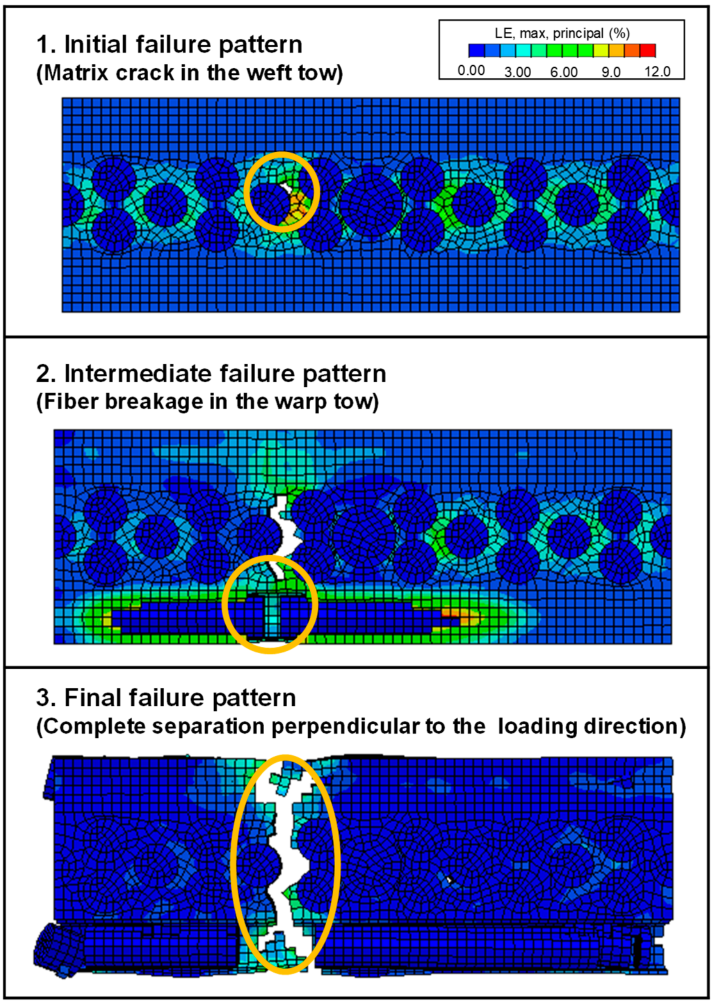

Figure 18. Progressive failure pattern of composite.

Although the failure patterns are the same across all the loading rates, FEA finds that the strains at the failure initiation in the matrix material are different at different loading rates. At 5 mm/min and 800 mm/min, matrix cracking in the weft tow occurs at a strain of $\varepsilon = 1.49\%$ and $\varepsilon = 1.38\%$, respectively, along the stress–strain curves in Figure 17. The higher loading rate increases the brittleness of the epoxy, leading to the failure onset in the matrix material at the lower strain level. The following intermediate failure patterns in Figure 18 are found at $\varepsilon = 1.50\%$ for 5 mm/min and $\varepsilon = 1.41\%$ for 800 mm/min. These findings suggest that the increased brittleness of the epoxy at higher loading rates results in the increase in the brittleness of the composite.

5. Conclusions

This study conducted tensile experiments and micro-scale FEA to investigate the tensile response of epoxy and plain weave carbon fabric-reinforced epoxy composites under varying loading rates. The primary objective was to investigate how changes in the mechanical behavior of epoxy, induced by loading rate, affect the mechanical behavior and failure mechanisms of the composite. The following key findings were established:

First, tensile experiments revealed that both epoxy and the composite exhibited increased brittleness with higher loading rates, while stiffness remained largely unchanged. Notably, despite the rate independence of the carbon fibers, the composite, like the epoxy, showed no significant change in stiffness but exhibited increased brittleness with higher loading rates. This suggests that the rate dependency of the epoxy has a significant influence on the rate dependency of the composite.

Second, the application of the acceleration model effectively reduced analysis time while validating the impact of the increased brittleness of the epoxy on the composite's brittleness. To observe the progressive failure pattern of the composite, the fiber diameter was enlarged, and the model was simplified. This led to differences between the maximum stress in experiments and simulations. However, the reduction in elongation and strength of the composite due to the increased brittleness of the epoxy at higher loading rates showed a good correlation between the tests and simulations.

The analysis of the progressive failure pattern confirmed the mechanism by which the increased brittleness of the epoxy contributed to the brittleness of the composite. At all loading rates, the composite failure progressed in three distinct stages. In the first stage, matrix cracking occurred in the weft tow; in the second stage, fiber breakage took place in the warp tow; and in the final stage, the composite fractured fully perpendicular to the loading direction. This failure mechanism, involving matrix cracking in the weft tow and fiber breakage in the warp tow as the primary processes, was consistent with the fracture surfaces observed in the experiments. As the loading rate increased, the increased brittleness of epoxy caused both matrix cracking and fiber breakage to occur at lower strain levels, leading to a reduction in the elongation and strength of the composite.

The numerical results were obtained from the simplified FE model. The microstructural geometries were intentionally simplified to enhance the effects of the matrix material. However, the simplified FE model still contained primary microstructural features. The FE model had nearly the same fiber volume fraction. The complex distribution of the fibers was modeled through the slightly enlarged center fiber. In this way, non-uniform stress distribution due to the complex fiber distribution could be captured in the simulations. Voids were not considered in the model because they were not observed. Fiber-matrix interfaces were modeled as a part of the matrix material. Rate-dependent interfacial behavior may be added to the FE model after its properties are characterized as proposed in [29,30].

This study demonstrates that the rate dependency of the epoxy directly influences the rate dependency of the composite. Moreover, it confirms that the rate dependency of the composite varies according to the rate dependency of the matrix epoxy. These findings provide crucial data for predicting and optimizing composite performance under various loading conditions and offer a valuable foundation for composite design in dynamic environments.

Author Contributions: T.C.: methodology, analysis, investigation, data curation, software, visualization, and writing—original draft preparation.; W.J.: conceptualization and supervision, writing—review and editing. All authors have read and agreed to the published version of the manuscript.

Funding: This work was financially supported through the Machinery and Equipment Program funded by the Ministry of Trade, Industry, and Energy (MOTIE) of the Republic of Korea (Grant No.: 20018217) and by the National Research Foundation of Korea grant funded by the Ministry of Science and ICT (MSIT) of the Republic of Korea (Grant No.: 2017R1D1A1B03035011).

Data Availability Statement: Data will be made available on request.

Conflicts of Interest: The authors declare no conflict of interest.

References

1. Lamon, F.; Maragoni, L.; Carraro, P.A.; Quaresimin, M. Fatigue damage evolution in woven composites with different architectures. *Int. J. Fatigue* **2023**, *167*, 107365. [CrossRef]
2. Maragoni, L.; Modenato, G.; De Rossi, N.; Vescovi, L.; Quaresimin, M. Effect of fibre waviness on the compressive fatigue behavior of woven carbon/epoxy laminates. *Compos. Part B Eng.* **2020**, *199*, 108282. [CrossRef]
3. Vieille, B.; Chabchoub, M.; Gautrelet, C. Influence of matrix ductility and toughness on strain energy release rate and failure behavior of woven-ply reinforced thermoplastic structures at high temperature. *Compos. Part B Eng.* **2018**, *132*, 125–140. [CrossRef]
4. Foroutan, R.; Nemes, J.; Ghiasi, H.; Hubert, P. Experimental investigation of high strain-rate behaviour of fabric composites. *Compos. Struct.* **2013**, *106*, 264–269. [CrossRef]
5. Chung, K.; Ryou, H. Development of viscoelastic/rate-sensitive-plastic constitutive law for fiber-reinforced composites and its applications. Part I: Theory and material characterization. *Compos. Sci. Technol.* **2009**, *69*, 284–291. [CrossRef]
6. Elmahdy, A.; Verleysen, P. Tensile behavior of woven basalt fiber reinforced composites at high strain rates. *Polym. Test.* **2019**, *76*, 207–221. [CrossRef]
7. Naik, N.K.; Yernamma, P.; Thoram, N.M.; Gadipatri, R.; Kavala, V.R. High strain rate tensile behavior of woven fabric E-glass/epoxy composite. *Polym. Test.* **2010**, *29*, 14–22. [CrossRef]
8. Fitoussi, J.; Meraghni, F.; Jendli, Z.; Hug, G.; Baptiste, D. Experimental methodology for high strain-rates tensile behaviour analysis of polymer matrix composites. *Compos. Sci. Technol.* **2005**, *65*, 2174–2188. [CrossRef]
9. Zhang, X.; Shi, Y.; Li, Z.X. Experimental study on the tensile behavior of unidirectional and plain weave CFRP laminates under different strain rates. *Compos. Part B Eng.* **2019**, *164*, 524–536. [CrossRef]
10. Lu, J.; Zhu, P.; Ji, Q.; Cheng, Z. Experimental study of in-plane mechanical properties of carbon fibre woven composite at different strain rates. *Polym. Polym. Compos.* **2017**, *25*, 289–298. [CrossRef]
11. Ma, D.; Manes, A.; Amico, S.C.; Giglio, M. Ballistic strain-rate-dependent material modelling of glass-fibre woven composite based on the prediction of a meso-heterogeneous approach. *Compos. Struct.* **2019**, *216*, 187–200. [CrossRef]
12. Shafiei, E.; Kiasat, M.S.; Barbero, E.J. Rate-dependent viscoplastic modeling and experimental validation of woven glass/epoxy composite materials. *Compos. Part B Eng.* **2021**, *216*, 108827. [CrossRef]
13. Zhou, Y.; Jiang, D.; Xia, Y. Tensile mechanical behavior of T300 and M40J fiber bundles at different strain rate. *J. Mater. Sci.* **2001**, *36*, 919–922. [CrossRef]
14. Czaderski, C.; Martinelli, E.; Michels, J.; Motavalli, M. Effect of curing conditions on strength development in an epoxy resin for structural strengthening. *Compos. Part B Eng.* **2012**, *43*, 398–410. [CrossRef]
15. Lapique, F.; Redford, K. Curing effects on viscosity and mechanical properties of a commercial epoxy resin adhesive. *Int. J. Adhes. Adhes.* **2002**, *22*, 337–346. [CrossRef]
16. ASTM International. *Standard Test Method for Tensile Properties of Plastics*; ASTM International: West Conshohocken, PA, USA, 2014.
17. Sause, M.G.; Sause, M.G. Digital image correlation. In *In Situ Monitoring of Fiber-Reinforced Composites: Theory, Basic Concepts, Methods, and Applications*; Springer: Cham, Switzerland, 2016; pp. 57–129.
18. Choi, H. Thermo-Mechanical Behavior of a Plain Woven Textile Composite Material: Experimental and Numerical Studies. Master's Thesis, Graduate School of UNIST, Ulsan, Republic of Korea, 2017.
19. *ABAQUS Analysis User's Manual, Version 2024*; Dassault Systèmes SE: Vélizy-Villacoublay, France, 2024.
20. Johnson, G.R. A constitutive model and data for metals subjected to large strains, high strain rates and high temperatures. In Proceedings of the 7th International Symposium on Ballistics, The Hague, The Netherlands, 19–21 April 1983.
21. Shadlou, S.; Ahmadi-Moghadam, B.; Taheri, F. The effect of strain-rate on the tensile and compressive behavior of graphene reinforced epoxy/nanocomposites. *Mater. Des.* **2014**, *59*, 439–447. [CrossRef]
22. Chen, W.; Zhou, B. Constitutive behavior of Epon 828/T-403 at various strain rates. *Mech. Time-Depend. Mater.* **1998**, *2*, 103–111. [CrossRef]
23. Yerramalli, C.S.; Sumant, C.; Prusty, R.K.; Ray, B.C. Finite element modelling and experimentation of plain weave glass/epoxy composites under high strain-rate compression loading for estimation of Johnson-Cook model parameters. *Int. J. Impact Eng.* **2022**, *167*, 104262.

24. Johnson, G.R.; Cook, W.H. Fracture characteristics of three metals subjected to various strains, strain rates, temperatures and pressures. *Eng. Fract. Mech.* **1985**, *21*, 31–48. [CrossRef]
25. Cantwell, W.J.; Roulin-Moloney, A.C.; Kaiser, T. Fractography of unfilled and particulate-filled epoxy resins. *J. Mater. Sci.* **1988**, *23*, 1615–1631. [CrossRef]
26. Toray Composites Materials America, Inc. *T300 Technical Data Sheet*; Updated 13 April 2018; Toray Composites Materials America, Inc.: Decatur, AL, USA, 2018.
27. Ma, H.; Aravand, M.A.; Falzon, B.G. Phase morphology and mechanical properties of polyetherimide modified epoxy resins: A comparative study. *Polymer* **2019**, *179*, 121640. [CrossRef]
28. Kant, M.; Penumadu, D. Fracture behavior of individual carbon fibers in tension using nano-fabricated notches. *Compos. Sci. Technol.* **2013**, *89*, 83–88. [CrossRef]
29. Koyanagi, J.; Ogihara, S.; Nakatani, H.; Okabe, T.; Yoneyama, S. Mechanical properties of fiber/matrix interface in polymer matrix composites. *Adv. Compos. Mater.* **2014**, *23*, 551–570. [CrossRef]
30. Tamrakar, S.; Haque, B.Z.; Gillespie, J.W. High rate test metho for fiber-matrix interface characterization. *Polym. Test.* **2016**, *52*, 174–183. [CrossRef]